Chip-Scale Molecular Clock

Cheng Wang, *Student Member, IEEE*, Xiang Yi, *Member, IEEE*, James Mawdsley, *Member, IEEE*, Mina Kim, *Member, IEEE*, Zhi Hu, *Student Member, IEEE*, Yaqing Zhang, Bradford Perkins, and Ruonan Han, *Member, IEEE*

Abstract—An ultra-stable time-keeping device is presented, which locks its output clock frequency to the rotational-mode transition of polar gaseous molecules. Based on a high-precision spectrometer in the sub-terahertz (THz) range, our new clocking scheme realizes not only fully electronic operation but also implementations using mainstream CMOS technology. Meanwhile, the small wavelength of probing wave and high absorption intensity of our adopted molecules (carbonyl sulfide, $^{16}O^{12}C^{32}S$) also enable miniaturization of the gas cell. All these result in an "atomic-clock-grade" frequency reference with small size, power, and cost. This paper provides the architectural and chip-design details of the first proof-of-concept molecular clock using a 65-nm CMOS bulk technology. Using a 231.061-GHz phase-locked loop (PLL) with frequency-shift keying (FSK) modulation and a sub-THz FET detector with integrated lock-in function, the chip probes the accurate transition frequency of carbonyl sulfide (OCS) gas inside a single-mode waveguide, and accordingly adjusts the 80-MHz output of a crystal oscillator. The clock consumes only 66 mW of dc power and has a measured Allan deviation of 3.8×10^{-10} at an averaging time of $\tau = 1000$ s.

Index Terms—Allan deviation, CMOS, frequency stability, GPS, molecular clock, navigation, carbonyl sulfide (OCS), rotational spectroscopy.

I. Introduction

FREQUENCY and timing references with high stability are essential to electronic systems. At present, electronic oscillators using high-Q quartz crystal and MEMS resonators are widely adopted [1]. They provide excellent phase noise and are suitable for systems such as portable radio and radar transceivers, which only require frequency stability within a short-term (<1 s). On the other hand, there is a vast application space where stability over a much longer time duration is needed. For example, positioning and navigation systems rely on their internal timestamps to determine the arrival time of satellite signals (in the case of GPS[1]) or the double integral of acceleration (in the case of inertial navigators). They are especially critical in situations where broadcasting signals for time service are unavailable, such as indoor operations, battle fields with electromagnetic spectral jamming, and underground/underwater sensing. As an example, in undersea reflection seismology for oil explorations [2], [3], where a large hydrophone sensor array detecting artificial seismic pulses is placed on the ocean floor, the timing error over the entire deployment duration of ~1 year should ideally be kept within $1 \sim 10$ ms; that requires sensor-integrated clocks with a long-term stability, quantified as Allan deviation [1], at 10^{-11} (or 10 ppt) level.

The frequency of a quartz crystal/MEMS oscillator is determined by the geometry and material properties of the resonator, hence having large sample-to-sample variability and susceptibility to environmental (e.g., temperature and acceleration) changes. To minimize the large drift (~100 ppm) of crystal oscillators over ~100°C temperature range, temperature-compensated crystal oscillators (TCXO) are extensively adopted [5], which incorporate temperature sensing and back-end frequency correction based on a pre-characterized temperature dependence. A TCXO typically consumes a few mW, but only reduces the drift to ppm level [6]. By enclosing the crystal in a temperature-stabilized oven chamber, an oven-controlled crystal oscillator (OCXO) further decreases the drift to ppb level [5]. This, however, comes at the expense of watt-level power consumption, a few minutes of warm-up time, and high cost (~\$100). Note that the above-mentioned timing devices also suffer from significant aging effect.

The ideal approach to address the above-mentioned stability problem is to reference the output frequency to a certain invariant physical constant. An atomic clock is based on such a principle by probing and locking to the hyperfine transition of electrons in, for example, cesium (^{133}Cs, $f_0 = 9.192631770$ GHz) and rubidium (^{87}Rb, $f_0 \approx 6.834682611$ GHz) atoms. Excellent stabilities at 10^{-11} to 10^{-18} levels are obtained from atomic clocks [4], [7]. Generally, these clocks are too bulky and costly for mainstream electronic systems; nevertheless, remarkable progress has been made in the miniaturization of atomic clocks over the past two decades. Utilizing a coherent-population trapping principle [8]

---

[1]Although by principle only three GPS satellites are needed for positioning, most mobile GPS receivers require the signal reception from more satellites to correct their internal clock timing with insufficient long-term stability.
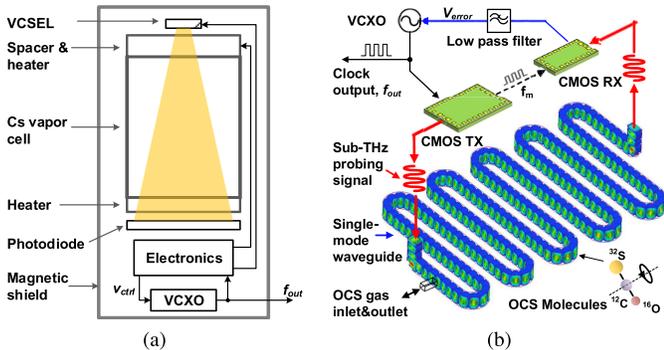
Fig. 1. Complexity comparison between implementations of (a) CSAC [4] and (b) CMOS molecular clock.

Fig. 2. Rotational energy levels of carbonyl sulfide ($^{16}O^{12}C^{32}S$), the transition frequencies, and the associated absorption intensities. A spectroscopic path length of 10 cm is assumed. The plot is based on the data from [25].

and advanced packaging technologies [9]–[11], cm^3-level atomic clocks [i.e., chip-scale atomic clocks (CSACs)] are demonstrated and deliver a frequency stability at 10^{-11} level (over an integration time τ of 1000 s to one day) while consuming ~0.12 W of power [12]. A typical CSAC diagram is shown in Fig. 1(a) [4]: in addition to a voltage-controlled crystal oscillator (VCXO) and clock electronics, it also contains a vertical-cavity surface-emitting laser (VCSEL)-photodiode spectrometer (for the optically-assisted probing of the Cs transition) and a cesium vapor cell tightly integrated with heaters (for evaporation of alkali metal and mK-level temperature stabilization for VCSEL). Moreover, since the 9.192631770-GHz line of Cs has a large second-order Zeeman drift with the presence of an external magnetic field ($\Delta f = 427$ Hz/G^2 or $\sigma = 4.6 \times 10^{-8}$/G^2 [13], [14]), a magnetic shield is also normally used. Such a complicated implementation leads to high cost (>\$1000) and degraded reliability [3], which have hindered the wide application of CSACs in mainstream, civil-grade systems.

This paper presents a new clock based on a fully electronic spectrometer, of which the output frequency is locked to the rotational-mode transition of carbonyl sulfide ($^{16}O^{12}C^{32}S$) gas molecules in the sub-terahertz (THz) range. THz rotational spectroscopy was primarily used for molecular identification in astronomy [15] and is recently explored for bio-medical diagnosis [16]–[18]. By applying it in a clock encapsulating certain pure gas sample, the needs for heaters, VCSEL, and photodiode in CSAC are eliminated. More importantly, we note that significant progresses in CMOS/SiGe-based THz spectrometers are made recently [19]–[21]. That opens up opportunities in building miniature molecular clocks with very low cost, size, and power. The diagram in Fig. 1(b) indicates not only a much simpler implementation of our chip-scale molecular clock but also the potentials of integrating it monolithically (except the gas cell) into a system-on-chip (SoC).

The physical principles of the molecular clock, as well as the demonstration of a lab-scale prototype with 2.2×10^{-11} stability ($\tau = 1000$ s), were recently described in [22]. In this paper, we present design details of the first molecular-clock CMOS chip [23] and related experimental data. By probing a transition line of carbonyl sulfide (OCS) molecules at 231.060983 GHz, the chip provides an Allan deviation of
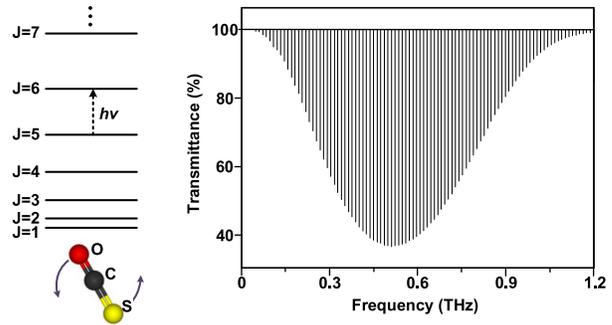
3.8×10^{-10} ($\tau = 1000$ s) while consuming only 66 mW of dc power. These preliminary data of the molecular clock indicate clear advantages over OCXOs and also well compare with CSACs. The remainder of this paper is organized as follows. In Section II, an overview of rotational spectroscopy and the line properties is given. In Section III, the architecture of the clock chip is presented. In Section IV, we discuss the design details of each circuit block and the clock packaging. Then, the experimental results, including the characterizations of a few circuit blocks and the stability of the entire clock, are provided in Section V. In Section VI, we conclude this paper with a comparison with the other state-of-the-art time-keeping devices.

II. FREQUENCY BASE OF THE CLOCK: ROTATIONAL SPECTRUM OF POLAR MOLECULES

We select a rotational spectral line of gaseous polyatomic molecules with a linear structure (e.g., carbonyl sulfide) as the reference of our clock. Compared to molecules with symmetric/asymmetric-top structures, linear molecules possess less rotational–vibrational coupling and fewer spectral lines adjacent to the line of our interest [24]. Note that each spectral line has finite linewidth, and if the tails of adjacent lines extend into the line under probing, the measured line profile becomes asymmetric and the line center frequency drifts when the gas pressure/temperature changes.

Similar to other behaviors of microscopic particles, the rotation of linear molecules has quantized energy levels (Fig. 2). For certain angular-momentum quantum number J, the rotational energy E_J follows a quadratic relationship [24]:

$$E_J = \frac{h^2}{8\pi^2 I} J(J+1) \tag{1}$$

where h is Planck's constant and I is the molecular moment of inertia about axes perpendicular to the internuclear axis. For an incident wave to be absorbed by the molecule, its photon energy should match the energy difference of E_J. Therefore, the associated transition frequency f_0 is

$$f_0 = f_{J+1 \Leftarrow J} = \frac{E_{J+1} - E_J}{h} = \frac{h}{4\pi^2 I}(J+1) \tag{2}$$

which indicates that the absorption spectrum consists of a set of equally spaced lines ($\Delta f = h/(4\pi^2 I)$). For $^{16}O^{12}C^{32}S$,

(a)

(b)

(c)
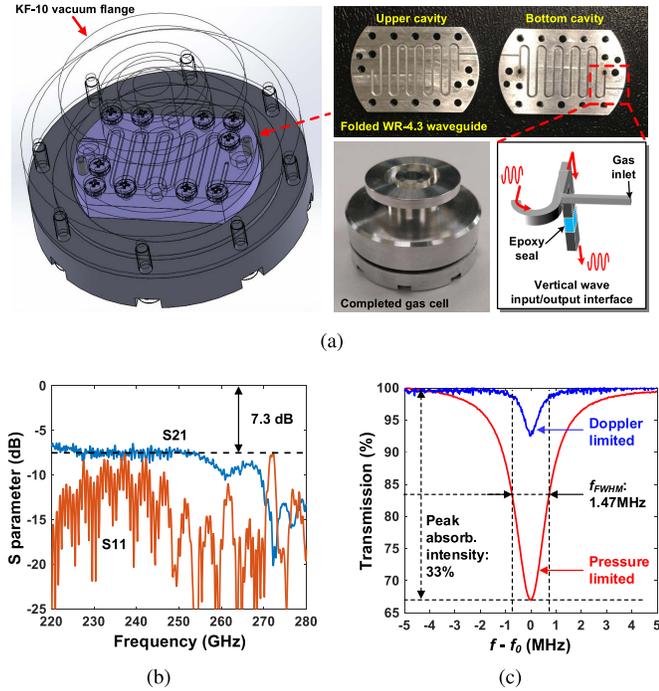
Fig. 3. (a) Custom-designed OCS gas cell for the clock prototype. (b) Measured S-parameters of the cell without gas. (c) Measured OCS transition line at $f_0 = 231.060983$ GHz with $\sim$1-μW probing power in the gas cell.

Δf is about 12.16 GHz [26]. Next, the absorption coefficient $\alpha_{\text{gas},J+1\Leftarrow J}$ is affected by two factors: first, each J angular momentum corresponds to $2J + 1$ degenerated sub-levels due to different orientations with magnetic quantum number $m_J = -J, -(J-1), \ldots -1, 0, 1, \ldots, J-1, J$; thus, rotational transition at higher frequency involves more quantum states contributing to absorption. Second, governed by Boltzmann's distribution, the probability of a molecule being at certain J state decreases exponentially with E_J. Those factors lead to

$$\alpha_{\text{gas},J+1\Leftarrow J} \propto (2J + 1) \cdot e^{-\frac{h^2 J(J+1)}{8\pi^2 I \cdot kT}}. \tag{3}$$

OCS is chosen also for its large dipole moment ($\mu_{\text{OCS}} \approx 0.7$ debye [25]), which leads to strong absorption $\alpha_{\text{gas},J+1\Leftarrow J}$. As shown in Fig. 2, the absorption of OCS firstly increases with frequency f_0, then peaks at $\sim$0.5 THz and finally decreases as f_0 rises toward 1 THz. Compared with those at lower frequencies, a spectral line at low-THz range provides adequate absorption via a short spectroscopic path length. Meanwhile, the clock gas cell, when shrunk into its minimum possible size, is a single-mode waveguide with a cross-sectional area proportional to $1/f_0^2$. As a result, higher f_0 enables gas cell miniaturization. In our work, the OCS transition line near 231.061 GHz ($J + 1 \Leftarrow J = 19 \Leftarrow 18$) is chosen, of which the absorption is already $0.6 \sim 0.7 \times$ of its peak value at $\sim$0.5 THz (Fig. 2). That achieves both small size of the gas cell and low power consumption of the CMOS electronics.

A gas cell based on a WR-4.3 rectangular waveguide is implemented [Fig. 3(a)]. The waveguide has a cross-sectional area of 1.092×0.546 mm^2 and a length of 140 mm—a

value that maximizes the signal-to-noise ratio (SNR) [18]. RF-transparent epoxy is used to seal OCS gas with a volume of 83 mm^3. A meandering shape of waveguide is adopted for gas cell miniaturization, which results in a clock volume limit of $\sim$1 cm^3. As shown in Fig. 3(b), the measured loss of the gas cell without OCS is 7.3 dB. Next, with OCS gas filling, a measured spectral line at 231.060983 GHz is shown in Fig. 3(c). With a gas pressure of 1 Pa, the Doppler-limited full-width at half-maximum (FWHM) is 0.65 MHz ($Q = 3.6 \times 10^5$), and the peak absorption intensity is 7%. With a pressure of 10 Pa, the FWHM is 1.47 MHz ($Q = 1.6 \times 10^5$) and is dominated by pressure broadening; the peak absorption intensity is 33%. For our clock, the pressure of 10 Pa is selected to optimize the Q–SNR product in (8). More information and experimental data regarding the spectral line properties (e.g., various spectral broadening and shifting mechanisms) can be found in [22].

III. DYNAMIC FREQUENCY COMPENSATION SCHEME AND CLOCK STABILITY

Similar to CSACs [Fig. 1(a)], the molecular clock performs closed-loop dynamic frequency correction to an off-chip VCXO. A simplified schematic is shown in Fig. 4(a). A THz phase-locked loop (PLL) referenced to the VCXO generates a probing signal with center frequency f_p. To detect the frequency error between f_p and the spectral line center f_0, frequency-shift keying (FSK) is adopted, with modulation frequency f_m and frequency deviation[2] Δf. As a result, the instantaneous frequency of probing signal is periodically toggled between $f_p + \Delta f$ and f_p-Δf. If $f_p \neq f_0$, the gas absorption is different between the two half duty cycles, as shown in Fig. 4(b). A square-law detector then extracts the envelope fluctuation V_{BB} of THz probing signal, and the amplitude and phase of V_{BB} correspond to the instantaneous offset $f_p - f_0$. Eventually, an error signal V_{error} derived from a lock-in detection [Fig. 4(a)] is used to adjust the frequency f_{XO} of VCXO. The loop settles when V_{error} is zero, and f_{XO}, which locks to f_0 (through a preset frequency division ratio), is used as the clock output.

The switch S_0 is on for normal clock operations. If the switch S_0 in Fig. 4(a) is off, a spectroscopic dispersion curve [Fig. 5(a)] is obtained by recording V_{error} while scanning the center frequency f_p of the FSK-modulated probing signal. The zero-crossing point ($f_p - f_0 = 0$) of the dispersion curve aligns with the spectral line center. Thus, when the feedback loop settles, the clock locks at that zero-crossing point. Note that in order to reduce the frequency error $f_p - f_0$, sufficiently large open-loop gain

$$G_L = MK_{\text{VCXO}}K_r G \tag{4}$$

is required. In (4), M is the frequency multiplication factor of PLL, K_{VCXO} (unit: Hz/V) is the voltage-tuning response of VCXO, K_r (unit: V/Hz) is the slope of the dispersion curve at $f_p - f_0 = 0$, and G is the additional voltage gain at baseband.

[2]Note that the modulation frequency f_m is much smaller than Δf, in order to concentrate the probing power within the spectral width of the transition line.

(a)

(b)
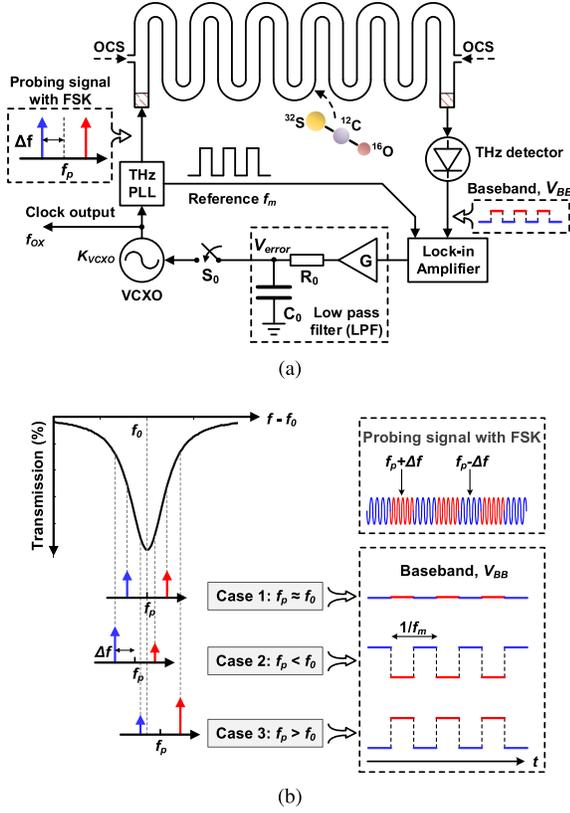
Fig. 4. (a) Simplified schematic of molecular clock. (b) Clock probing scheme using an FSK-modulated signal in the sub-THz range.

(a)

(b)

(c)

Fig. 5. (a) Measured dispersion curve of OCS at $f_0 = 231.060983$ GHz using instruments. (b) Simulated dispersion curves under different frequency deviation Δf. (c) Simulated slope of dispersion curve at the zero-crossing point K_r versus Δf.

Due to the noise on the dispersion curve, the zero-crossing point fluctuates over time. The corresponding short-term frequency instability [Fig. 5(a)] is then obtained as $f_p - f_0 = V_n/K_r$, where V_n is the root-mean-square (rms) noise of the dispersion curve. According to the previous studies [24], [27], [28], such frequency instability of a passive clock, defined as Allan deviation σ_y, is determined by

$$\sigma_y(\tau) = \frac{V_n}{K_r \cdot f_0 \cdot \sqrt{2\tau}} \qquad (5)$$

where τ is the averaging time. In our clock, V_n is dominated by the noise of the sub-THz receiver; therefore, the increase in K_r is needed to improve the short-term stability. Note that K_r is determined by not only the probing power, absorption intensity, and quality factor of spectral line but also the frequency deviation Δf of FSK modulation, as shown in Fig. 5(b). In the Appendix [see (15)], the optimal Δf is derived to be $\Delta f_{opt} = 0.29 \cdot f_{FWHM}$, which is also validated by the simulation in Fig. 5(c). Using such a frequency deviation, the peak value of the dispersion curve is $V_{error,max} \approx 0.23 \cdot K_r \cdot f_{FWHM}$ [see (17) in the Appendix].

Finally, we define the quality factor Q and the $SNR_{v/v}$ of a spectral line as

$$Q = \frac{f_0}{f_{FWHM}} \qquad (6)$$

and

$$SNR = \frac{V_{error,max}}{V_n} \approx \frac{0.23 \cdot K_r \cdot f_{FWHM}}{V_n} \qquad (7)$$

respectively. Using (6) and (7), the Allan deviation of molecular clock in (5) can be re-expressed based on the Q–SNR product of the dispersion curve

$$
\sigma_y(\tau) \approx \frac{V_n}{\left(\frac{V_n \cdot SNR}{0.23 f_{FWHM}}\right) \cdot (Q \cdot f_{FWHM}) \cdot \sqrt{2\tau}}
$$
$$
= \frac{0.17}{Q \cdot SNR \cdot \sqrt{\tau}}. \qquad (8)
$$

Note that (8) is valid only if the frequency deviation of the FSK-modulated probing signal is set to Δf_{opt} and $\Delta f_{opt} \gg f_m$. Finally, we point out that for the feedback control loop of the clock to converge correctly, the slope of the spectrometer-probed dispersion curve should be positive at any moment. That means the initial offset of the probing frequency f_p should be within $\pm f_{e,peak}$ [Fig. 5(a)], where $f_{e,peak}$ is the frequency at which the dispersion curve reaches its peak value and is derived to be $0.38 f_{FWHM}$ [see (16) in the Appendix]. For the OCS line shown in Fig. 3(c), $0.38 f_{FWHM}$ is related to a frequency tolerance of ± 2.4 ppm. Thus, the start-up condition of the clock can be achieved with either a TCXO or a startup process involving a rough search of the zero-crossing point followed by the setting of the initial frequency of a VCXO.

IV. MOLECULAR CLOCK ON CMOS

A pair of CMOS transmitter (TX) and receiver (RX) chips, with an architecture shown in Fig. 6, is implemented to realize the above-mentioned frequency regulations to
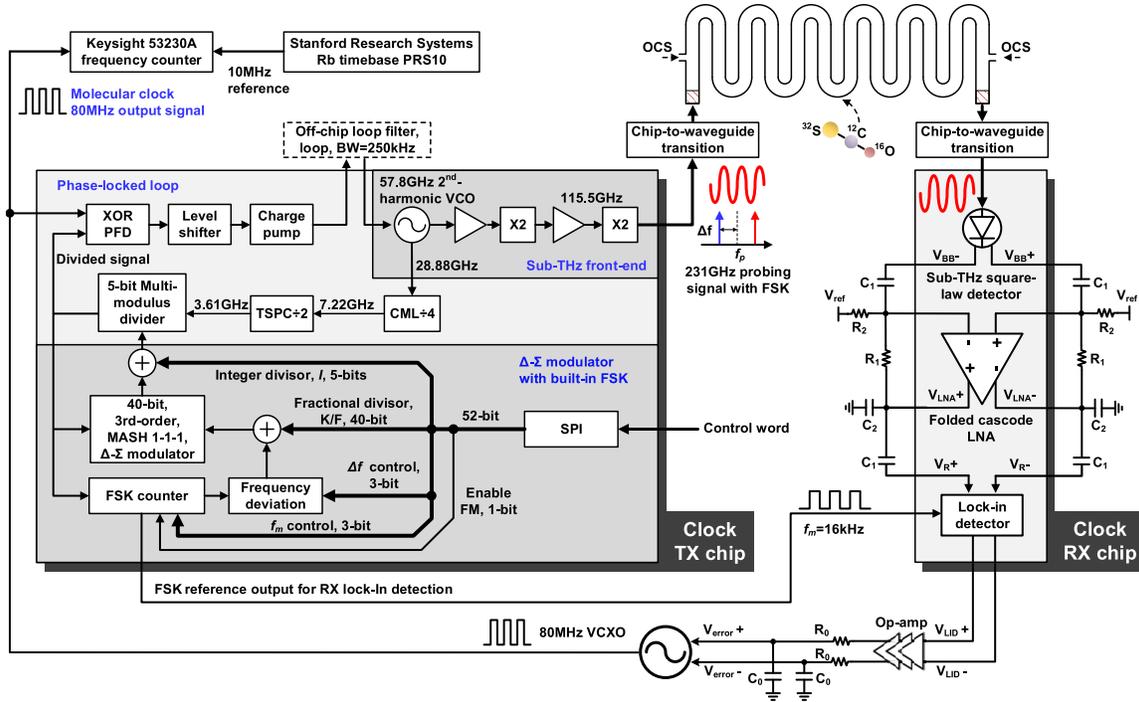
Fig. 6.   Architecture and block diagram of the CMOS molecular clock chipset.

an 80-MHz VCXO. The separation of the TX and RX is to facilitate the packaging of this first prototype and to avoid any undesired coupling of sub-THz signal through the silicon substrate. The latter may cause large tilting of the spectroscopic baseline and output frequency drift [22]. Nevertheless, a single-chip implementation of the molecular clock is still possible in the future.

A. Clock Transmitter: Generation of Sub-THz Probing Signal

On the TX chip, the 231.061-GHz probing signal is generated by a sub-THz front end, which consists of a 57.8-GHz harmonic voltage-controlled oscillator (VCO), two cascaded frequency doublers, and inter-stage amplifiers. The 28.9-GHz fundamental oscillation of the harmonic VCO is also divided down to establish a fractional-N PLL, which locks to an 80-MHz VCXO. The PLL contains a 5-bit multi-modulus divider, which is modulated by a 40-bit, third-order multi-stage noise shaping (MASH) 1-1-1 Δ-Σ modulator. This modulator enables a frequency-tuning resolution of 10^{-12} ($\sim$0.2 Hz at 231 GHz and $\sim$0.1 mHz at 80 MHz), which is used for high-accuracy calibration of the output frequency.[3] The fractional divisor K/F of Δ-Σ is periodically reset by an on-chip digital counter to implement the FSK modulation. The loop bandwidth of the 40-bit fractional-N PLL and the modulation frequency are selected to be 250 and 16 kHz, respectively. According to our experiments, these two parameter values maximize the SNR of the measured spectral line

[3]Note that the previous experimental works [29], [30] were only able to determine the OCS transition frequency with kHz-level accuracy. Therefore, the exact PLL division ratio needed for an 80-MHz clock output with $<10^{-9}$ accuracy can only be derived during our testing.

and the short-term stability of clock. Note that low f_m leads to excessive flicker noise in the THz detector, and high f_m leads to shorter length and less randomness of the control code for the multi-modulus divider in the PLL during FSK modulation (hence, larger frequency error). Meanwhile, the PLL loop bandwidth should be sufficiently high to support the FSK modulation. The integer divisor I, fractional divisor K/F (40-bit), FSK modulation frequency f_m (3-bit), frequency deviation Δf (3-bit), and an FM enabler (1-bit) are set externally through a serial-to-parallel data interface (SPI).

Fig. 7 shows the 3-D structure and detailed schematic of the 231-GHz transmitter front end. Note that in contrast to prior THz gas-sensing setups [19]–[21], the waveguide gas cell used in our clock highly confines the THz power, which may cause power saturation of OCS molecules and broaden the spectral line [24]. Our study [22] indicated that an injected probing power of $\sim$50 μW leads to the highest Q–SNR product. Such a power level is feasible for low-power operation using mainstream CMOS technologies. We use a millimeter-wave VCO cascaded with a sub-THz multiplier chain, instead of a sub-THz VCO plus a sub-THz divider chain, due to the following advantages of former scheme: 1) lower total power consumption, which dominates the dc power of the entire clock; 2) reduced amplitude (AM) noise due to the voltage-clipping effects of the multipliers, which are heavily driven into saturation; and 3) wide VCO tuning range Δf_T to cover the target spectral line; Δf_T should be larger than the 12.16-GHz frequency spacing of OCS spectrum (Fig. 2). The VCO adopts a cross-coupled structure and oscillates at 28.88-GHz fundamental frequency. The common-mode second-harmonic signal at 57.8 GHz is then extracted from the top of VCO. The two cascaded frequency doublers with
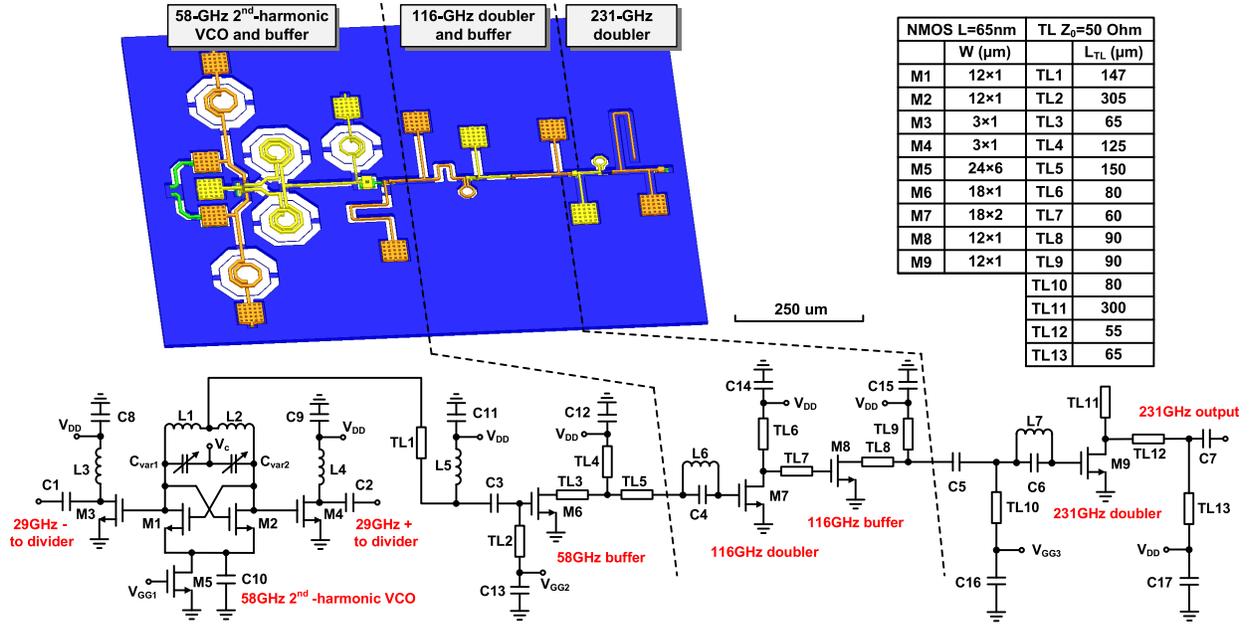
Fig. 7. Second-harmonic VCO and frequency multiplier chain of the TX: 3-D structure (top) and circuit schematic (bottom).

output frequency at 116 and 231 GHz, respectively, are realized using NMOS transistors biased close to the threshold voltage. Two resonators (L_6 and C_4, L_7 and C_6) reject the backward propagation of the second-harmonic signals generated from the drains of transistor and leaked through their C_{gd}. No feedback structure [31] is adopted here for power saving. Two inter-stage buffers with common-source NMOS are implemented to provide sufficient driving power. The simulation of the sub-THz front end shows a peak output power of -9.1 dBm at 231.9 GHz with a 3-dB bandwidth of 18.6 GHz.

B. Sub-THz Receiver With Integrated Lock-In Detection

Fig. 8 presents the schematic of the RX chip. The envelope fluctuation of probing signal induced by the OCS absorption [Fig. 4(b)] is obtained by a 231-GHz pseudo-differential square-law detector based on an NMOS transistor. The input signal applied at the gate and drain (through C_{gd}) of the device undergoes a self-mixing process. The NMOS is biased in the sub-threshold regime for the reduction of flicker noise. The simulated detector responsivity is 5.0 kV/W and the noise equivalent power (NEP) is 48 pW/Hz$^{0.5}$ at a baseband frequency of 16 kHz. The extracted baseband signal V_{BB} is then amplified by a differential low-noise amplifier. Using a single-stage folded-cascode topology, the amplifier has a simulated gain of 55 dB. At the baseband frequency of 16 kHz, the amplifier has an input-referred noise of 20 nV/Hz$^{0.5}$, which is much lower than the 228-nV/Hz$^{0.5}$ output noise of the preceding square-law detector.

Next, the demodulation of the baseband signal is achieved by an integrated lock-in detector. The reference clock of the lock-in detector (FSK and $\overline{FSK}$ in Fig. 8) comes from the phase-aligned digital signal of the TX chip at the modulation frequency ($f_m = 16$ kHz, see Fig. 6). Based on a bank of
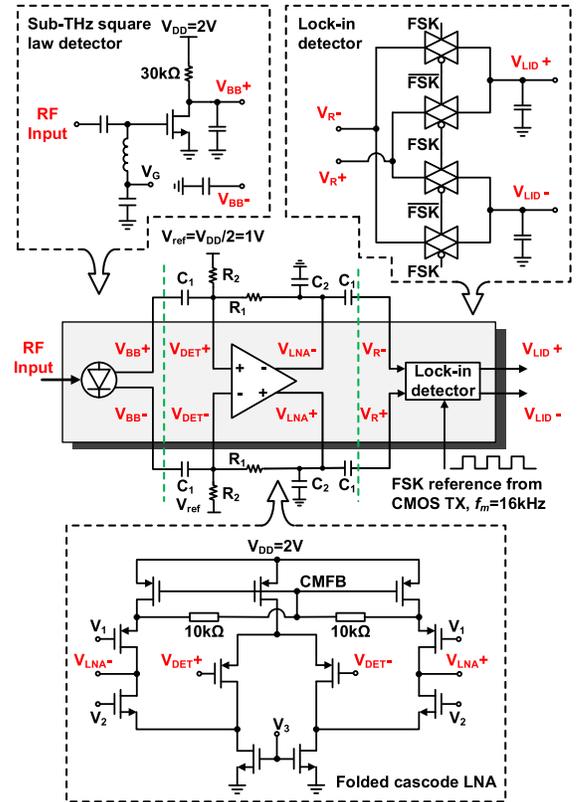
Fig. 8. Schematic of the molecular clock receiver (RX).

transmission gates feeding to an amplifier and a low-pass filter [32], the lock-in detector performs a narrowband (hence low-noise) down-conversion of the envelope fluctuation V_{BB} into a dc error signal V_{error}. As described in Section III, V_{error} represents the frequency difference between the instantaneous probing frequency f_p and the spectral line center f_0.
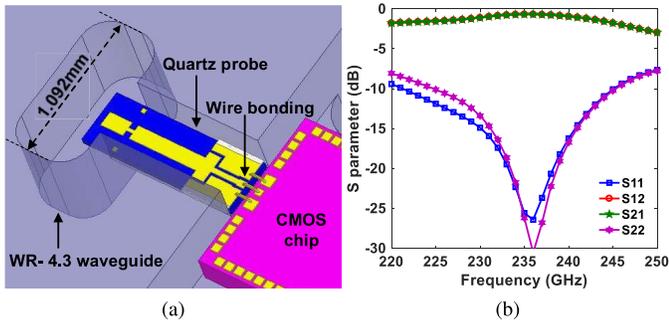
Fig. 9. Design of the 231-GHz chip-to-waveguide coupler: (a) 3-D structure for electromagnetic simulations and (b) simulated S-parameters.

V_{error} is eventually used to control the 80-MHz VCXO; hence, a dynamic frequency-compensation loop is established.

It is noteworthy that the heterodyne detection scheme is not adopted by the clock receiver. In a radio or radar system, heterodyne detection is typically much more sensitive than direct detection, because the input RF power of the receiver is much smaller than the local oscillation (LO) power; therefore, a heterodyne mixing leads to an output signal much larger than that from the self-mixing in a square-law detector. In a spectroscopic system, however, the receiver input power is much larger, hence heterodyne detection is less effective in SNR enhancement. In addition, direct detection does not require LO signal and is, therefore, much more power efficient.

C. Chip-to-Waveguide Signal Coupling

Two chip-to-waveguide couplers are implemented to establish the THz signal connections between the CMOS TX/RX chips and the WR-4.3 waveguide gas cell. As shown in Fig. 9(a), the coupler is based on a microstrip line to waveguide probe structure [33]. The probe is fabricated on a fused quartz substrate with a thickness of 50 μm and a relative dielectric constant of 3.8. Based on 3.5-μm-thick gold, the metal pattern turns the quasi-TEM signal at the microstrip side into a TE-mode wave at its extension into the vertical waveguide. Three bond wires forming a ground–signal–ground transmission line are used to connect the chip with the quartz probe. Impedance matching using a step-impedance stripline is designed to further reduce the reflection due to the inductance of the bond wires. The simulated S-parameters of the coupler are shown in Fig. 9(b), which indicate an insertion loss of ~1.0 dB at 231 GHz and a 3-dB bandwidth over 30 GHz.

V. CHIP PROTOTYPE AND EXPERIMENTAL RESULTS

The clock chipset is fabricated using a TSMC 65-nm CMOS low-power (LP) technology ($f_{max} \approx 220$ GHz). Fig. 10 shows the micrographs of the chips, as well as the packaging of the molecular clock module. The module consists of the following: 1) an atmospheric-pressure metal cavity, which houses the TX/RX chips and printed circuit board (PCB) and 2) a bottle-cap-sized metal chamber, which houses the waveguide gas cell. The chamber is also connected to a vacuum pumping system via a KF-10 flange for low-pressure (~10 Pa) OCS
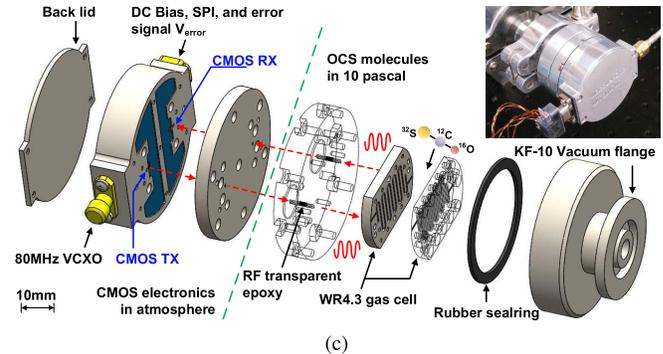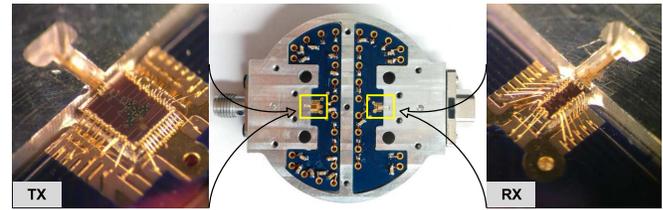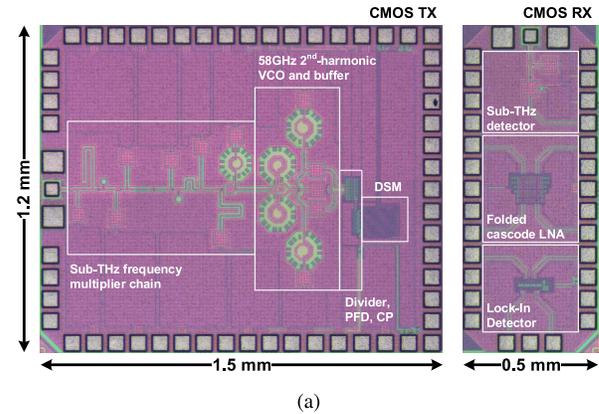
Fig. 10. Packaged molecular clock module. (a) Photographs of TX and RX chips. (b) Wire-bonded chips and chip-to-waveguide couplers. (c) Details of the clock assembly.

gas injection. As is shown in Figs. 3(a) and 10(c), the above-mentioned two parts of the clock module are separated by RF-transparent epoxy filled inside two short (~1 mm) sections of the waveguide near the chips.

A. Measurement Results of CMOS TX/RX Chips

A custom-designed VCXO on PCB provides the 80-MHz reference for the PLL in TX. After phase locking, the power of the sub-THz output from the TX is measured by a Virginia Diode Inc. (VDI) Erickson PM-5 power meter connected to the WR-4.3 waveguide flange of the packaged molecular clock module. As shown in Fig. 11(a), the output power reaches −20.2 dBm with an 18-GHz tunable bandwidth. Note that these data include the loss of the chip-to-waveguide coupler. Next, a VDI even-harmonic mixer (EHM), driven by an LO signal at 14.424 GHz (16th-harmonic mixing), is utilized to down-convert the TX signal at $f_0 = 231.060983$ GHz to an inter-mediate frequency (IF) of 279 MHz. Fig. 11(b) shows the measured IF spectrum using

(a)

(b)
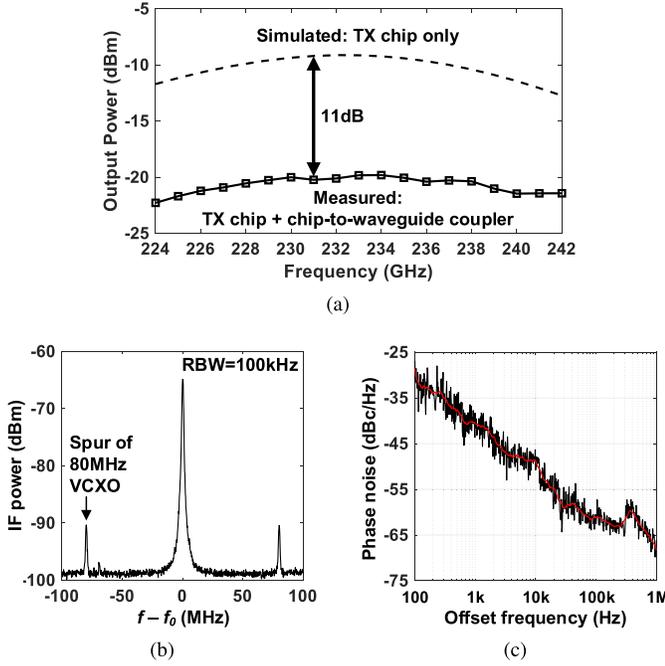
Fig. 11. Measurement results of the TX. (a) Output power at the waveguide interface. (b) Output spectrum without FSK modulation ($f_0 = 231.060983$ GHz). and (c) Corresponding phase noise of (b).

Fig. 12. Measured performance of RX (sub-THz square-law detector plus the LNA). (a) Total responsivity. (b) NEP.

Fig. 13. Power consumption of the clock components (total dc power of the clock chipset: 66 mW).

a spectrum analyzer (Keysight N9020A). The two sideband spurs are from the 80-MHz VCXO clock signal. The phase noise of the 231.061-GHz TX output is -68.4 dBc/Hz at 1-MHz frequency offset [Fig. 11(c)]. It refers to a phase noise of <-138 dBc/Hz at 1-MHz offset of the 80-MHz clock output. This is $\sim 10\times$ higher than other PLLs in a similar frequency range [34], [35]; but note that the dc power budget assigned for our clock transmitter is also $\sim 10\times$ lower than the above. We also note that the phase noise of the sub-THz signal may increase the baseband noise via a PM-to-AM noise conversion, due to the steep slope of the transition line [18]. The expected SNR, if it is only limited by the above-mentioned mechanism, is evaluated by the following equation (from [18]):

$$\text{SNR}_{\text{PN}} = \frac{f_{\text{FWHM}}}{f_m \sqrt{\text{PN}(f_m)}} \tag{9}$$

where $f_{\text{FWHM}} = 1.47$ MHz is the FWHM of rotational spectral line, $f_m = 16$ kHz is the modulation frequency, and $\text{PN}(f_m) = -53.6$ dBc/Hz at 16 kHz is the phase noise at the modulation frequency f_m. The calculated SNR_{PN} is 93 dB, which is much higher than the measured SNR to be shown next. Hence, the short-term stability of our clock chip is currently not limited by the phase noise.

Next, an amplitude-modulated sub-THz signal generated by a VDI frequency extender is injected into the RX chip. The injected power is calibrated by the PM-5 power meter. A lock-in amplifier (Stanford Research Systems SR865A) measures the responsivity R_v (unit: V/W) of RX, including the waveguide-to-chip coupler, sub-THz square-law detector, and on-chip LNA. Meanwhile, the output noise spectral density V_n (unit: V/Hz$^{0.5}$) of RX is also measured, which then gives the NEP as NEP $= V_n/R_v$. At the baseband frequency of 16 kHz,

the measured responsivity is 1.8×10^5 V/W [Fig. 12(a)] and the measured NEP is 501 pW/Hz$^{0.5}$ [Fig. 12(b)]. Due to the dominance of the flicker noise from the NMOS detector, higher baseband frequency (i.e., FSK modulation frequency f_m) is preferable. However, as mentioned earlier, f_m is selected to be 16 kHz considering the tradeoff between the flicker noise in RX and the accuracy of FSK modulation in TX.

According to the simulation–measurement comparisons in Figs. 11(a) and 12(b), we suspect that an excessive insertion loss of ~ 10 dB exists in each chip-to-waveguide coupler at 231 GHz. That may due to the overlength of the bond wires, as well as the wave absorption into the thick (~ 300 μm) silicon substrate exposed to the coupler. The problem will be further investigated and addressed in the future. Finally+, the total power consumption of TX and RX chips is 66 mW, 70% of which comes from the second-harmonic VCO and sub-THz multiplier chain (Fig. 13). The RX chip only consumes 3 mW of power.

B. Performance Characterization of CMOS Molecular Clock

With OCS gas injected into the WR-4.3 gas cell, the dispersion curve of the transition line is measured as the first step of clock performance characterization. This is achieved by as follows 1) performing FSK modulation and scanning of probing frequency f_p on the TX chip and 2) feeding the output of the folded-cascode LNA on the RX chip to a lock amplifier (SR865A), which references to the 16-kHz FSK modulation signal from the TX. From this open-loop configuration of the clock chipset, the lock-in amplifier reading V_{LID} as a function of f_p is obtained (Fig. 14). The measured SNR of the dispersion curve, under an OCS pressure of 10 Pa, is 445 in voltage or 53 dB in power.
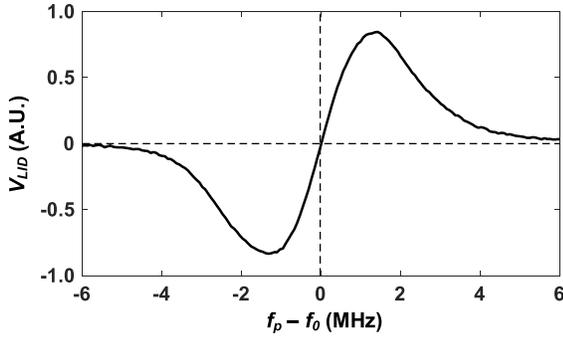
Fig. 14. Spectral dispersion curve of OCS ($f_0 = 231.060983$ GHz), measured entirely by the clock chipset with an open-loop configuration.
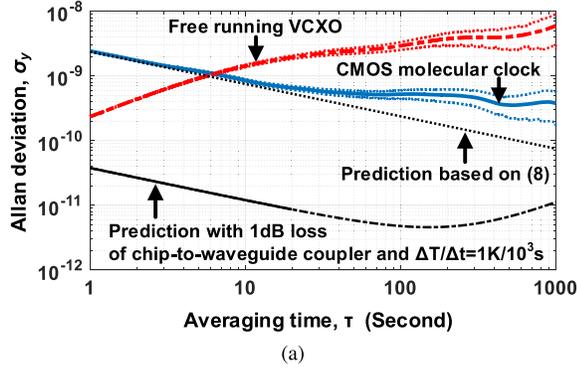
(a)
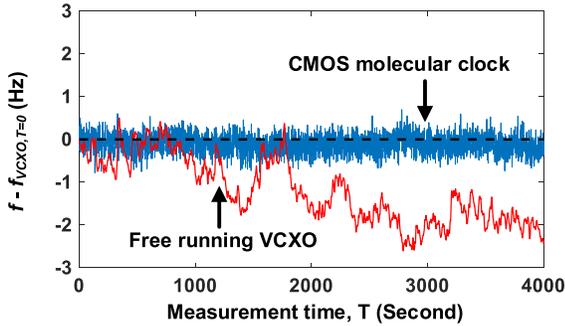
(b)

Fig. 15. Measured frequency stability of the molecular clock. (a) Overlapping Allan deviation σ_y. Dotted plots: confidence interval of the measurements. (b) Instantaneous frequency (sampled and integrated every 1 s) over 4000 s.

Next, to ensure initial locking, the output frequency of VCXO with the control terminal grounded is measured by a Keysight 53230A frequency counter referenced to a Stanford Research Systems rubidium atomic clock PRS10.[4] Then, the 40-bit control code of the fractional-N PLL is calculated so that the probing signal lands near the center of the OCS spectral line. Note that in our testing, we are concerned more about the clock stability than its accuracy; any output frequency offset (i.e., inaccuracy) can be easily calibrated later by changing the static control code of PLL after clock locking.

Finally, the CMOS molecular clock is configured with a closed loop: the output signal V_{LID} of the RX, which is demod-

[4]The same setup is also used later for the clock stability characterization, as is shown in Fig. 6. The PRS10 reference has an Allan deviation below 10^{-12} at $\tau = 1000$ s, which is sufficiently low to measure our molecular clock.
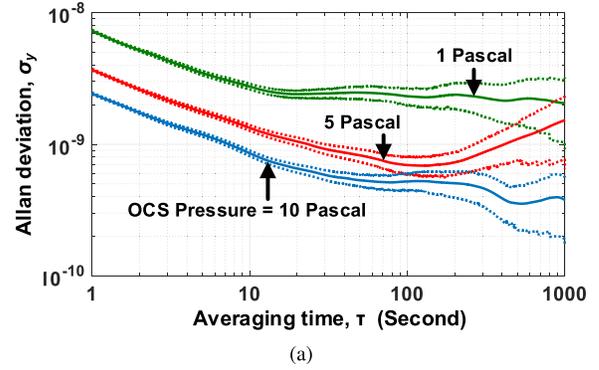
(a)
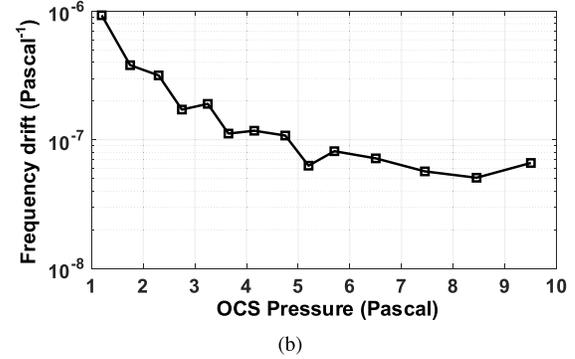
(b)

Fig. 16. Measured clock stability versus gas pressure. (a) Overlapping Allan deviation σ_y under 1-, 5-, and 10-Pa pressures of OCS. Dotted lines: confidence intervals. (b) Pressure-induced frequency drift.

ulated by the on-chip lock-in detector in Fig. 8, is fed into a low-pass filter ($R_0 = 50$ kΩ, $C_0 = 10$ μF, see Fig. 6), and then connected to the control terminal of VCXO. Fig. 15(a) shows the measured overlapping Allan deviation σ_y [1] when OCS pressure is 10 Pa. With an averaging time of 1000 s, σ_y reaches 3.8×10^{-10}. Comparing with the free-running VCXO, it enhances the long-term stability by 15×. This factor is expected to be larger with a greater change of environmental temperature. Note that the prediction in Fig. 15(a), which is based on (8), shows excellent agreement with the measurement in the short term ($\tau < 10$ s). Also, note that due to the degraded SNR of the measured OCS line, the clock exhibits higher fluctuation than the VCXO when $\tau < 6$ s. This is expected to be improved in the future. For example, Fig. 15(a) shows the predicted Allan deviation if the loss of each chip-to-waveguide coupler is reduced from 10 to 1 dB (the simulated value): the expected short-term σ_y at $\tau = 1$ s improves to 4×10^{-11}—this is the minimum short-term instability of the clock based on the presented CMOS chipset. Finally, Fig. 15(b) shows the measured instantaneous frequency of the CMOS molecular clock over 4000 s. It is obvious that the molecular clock feedback prevents the long-term VCXO frequency from drifting.

In addition, Fig. 16(a) presents the measured Allan deviations under different pressures of the OCS sample. Although OCS sample at 1 Pa has narrower linewidth compared with that at 10 Pa [$Q_{1\text{Pa}} = 3.6 \times 10^5$ versus $Q_{10\text{Pa}} = 1.6 \times 10^5$, see Fig. 3(c)], in our measurements, the latter provides 3× better short-term stability ($\tau < 10$ s) due to the enhanced Q–SNR product. Furthermore, the measured pressure-induced

TABLE I
COMPARISON OF FREQUENCY REFERENCES

References	Physics Principle	Allan Deviation	Turn-On Time (s)	DC Power (mW)	Implementation
[38]	Rubidium-Based CSAC ($f_{Rb} \approx 6.834683$ GHz)	3×10^{-10} ($\tau = 400$ s)	N/A	26^1	180-nm CMOS Chip + MEMS Gas Cell with Integrated Photonics
[12]	Cesiuim-Based CSAC ($f_{Cs} \approx 9.192632$ GHz)	1×10^{-11} ($\tau > 1000$ s)	~120	120	Discrete Electronics + MEMS Gas Cell with Integrated Photonics and Heater + Magnetic Shield
[39]	Ammonia Molecular Clock ($f_{NH_3} \approx 23.8701$ GHz)	2×10^{-10} ($\tau > 1000$ s)	<1	7500	Discrete Electronics + Microwave Waveguide
This Work	OCS Molecular Clock ($f_{OCS} \approx 231.060983$ GHz)	3.8×10^{-10} ($\tau = 1000$ s)	<1	66^2	65-nm CMOS Chip + Sub-THz Waveguide

[1]The power of off-chip heater, laser, and other components is not included.   [2]The power of the VCXO is not included.

frequency drift is shown in Fig. 16(b). At pressure of 10 Pa, the clock exhibits a pressure dependency of 6.6×10^{-8} Pa^{-1}. In our current prototype, the vacuum system exhibits a leakage rate <0.1 Pa/h, which leads to the long-term frequency drift in Fig. 15(a). This issue can be solved by using a hermetic gas cell, which is disconnected from the vacuum pump.

According to the gas law, the pressure change over temperature is 3.3×10^{-2} Pa/K (under 10-Pa pressure and 300-K temperature), which then leads to a clock temperature coefficient of 2.2×10^{-9} K^{-1}. This temperature dependency, however, is mainly due to the non-flat spectroscopic baseline of the packaged clock module [22], rather than the intrinsic temperature-induced drift of OCS transition frequency; the latter is $\sim 1 \times 10^{-11}$ K^{-1} or below [22], [36]. The temperature-induced frequency drift is due to the variation of mean free time of inter-molecular collision under pressure change and velocity dependency of the collision cross section. Hence, assuming a temperature variation rate of $\Delta T / \Delta t = 1$ K/$10^3 s$, a long-term stability of 1×10^{-11} with $\tau = 10^3$ s is expected, as shown in Fig. 15(a). In addition, Fig. 16(a) shows that the pressure-induced drift is more severe at lower pressure because the impact of the baseline tilting is more predominant when OCS absorption is weak. Note that such impacts (hence, the temperature dependency) can be effectively reduced by probing high-order dispersion curves in the clock-feedback loop, which was demonstrated in the lab-scale clock in [22].

Besides temperature/pressure dependency, there are also other factors leading to long-term frequency drift, such as: 1) drift of free-running VCXO, which can be suppressed by sufficiently high clock loop gain; 2) Zeeman effect, which refers to σ-component doublet splitting caused by magnetic field. The magnetic-induced shift is about 1×10^{-10} G^{-1} for the 231.061-GHz spectral line. Thus, a magnetic field shielding structure such as that used in CSACs is unnecessary; and (3) Stark effect, which refers to asymmetric frequency shifts of the sublevels due to the existence of external electrical field. Note that 10% fluctuation of RF power only causes a relative drift of 1×10^{-13}. Further information about the long-term stability can be found in [22], [24], and [26].

VI. CONCLUSION

In this paper, an "atomic-clock-grade" miniaturized clock based on a mainstream 65-nm CMOS technology is described.

It is realized by referencing the electronic clock oscillation to the rotational-mode transition of OCS molecules at the sub-THz band. Table I compares this paper with the other relevant publications. Compared with ammonia clock utilizing inversion spectrum at K-band [38], the chip-scale molecular clock realizes miniaturization with the shorter wavelength. Although this chip-scale molecular clock is the first proof-of-concept, its long-term stability has already been competitive with that of rubidium clock [37]. With an improvement of the chip-waveguide signal coupling, the molecular clock should also be able to deliver 10^{-11}-level stability [Fig. 15(a)] as the cesium CSAC [12] does. Meanwhile, thanks to its all-electronic construction, the molecular clock greatly reduces the complexity and cost, which currently limit the wide applications of CSACs.

In the future, the OCS gas will be hermetically sealed inside the waveguide, so that no metal chamber nor connections to the vacuum system, shown in Fig. 10(c), are needed. In addition, efficient sub-THz waveguides can also be manufactured using low-cost silicon micromachined technology [39]. Such progresses will further reduce the volume of the clock to <1 cm^3. In conclusion, the presented chip-scale molecular clock has great potentials to be a highly stable frequency reference with small cost, size, and power, which is ideal for portable devices used in networked sensing, navigation, and communication and operations under GPS denial.

APPENDIX: OPTIMAL FREQUENCY DEVIATION OF THE FSK-MODULATED PROBING SIGNAL

In this section, we find the optimal frequency deviation Δf of the FSK-modulated probing signal, in order to maximize K_r in (5) (hence, the short-term stability). First, when the FSK modulation is off, the baseband signal V_{BB} is written as

$$V_{\text{BB}}(f_p) = R_r P_0 e^{-(\alpha_0 + \alpha_{\text{gas}, J+1 \Leftarrow J})L}$$
$$\approx R_r P_0 e^{-\alpha_0 L}(1 - \alpha_{\text{gas}, J+1 \Leftarrow J} \cdot L) \qquad (10)$$

where R_r is the responsivity of receiver, P_0 is the power of probing signal, α_0 is the loss of gas cell (without gas) per unit length, $\alpha_{\text{gas}, J+1 \Leftarrow J}$ is the absorption coefficient of spectral line per unit length, and L is the length of gas cell. Here, we assume $\alpha_{\text{gas}, J+1 \Leftarrow J} \cdot L \ll 1$. Next, under pressure broadening, the absorption coefficient $\alpha_{\text{gas}, J+1 \Leftarrow J}$ of spectral

line has a Lorentzian profile [24]

$$\alpha_{\text{gas},J+1 \leftarrow J}(f_p) \approx \beta \frac{1}{4(f_p - f_0)^2 + f_{\text{FWHM}}^2} \tag{11}$$

where

$$\beta = \frac{16\pi N_m f_L |\mu_{J,J+1}|^2 f_0^2 f_{\text{FWHM}}}{3ckT}. \tag{12}$$

In (12), N_m is the total number of molecules per unit volume, f_L is the fraction of molecules on the lower state of rotational transition, $\mu_{J,J+1}$ is the dipole moment for the transition from state J to state $J+1$, c is the speed of light, k is Boltzmann's constant, and T is the temperature. Therefore, after performing FSK modulation on the TX side and phase-aligned lock-in detection on the RX side, the induced error signal $V_{\text{error}}(f_e)$ is expressed as

$$
\begin{aligned}
V_{\text{error}}(f_e) &= V_{\text{BB}}(f_p + \Delta f) - V_{\text{BB}}(f_p - \Delta f) \\
&= R_r P_0 e^{-\alpha_0 L} \beta \Bigg[\frac{1}{4(f_e - \Delta f)^2 + f_{\text{FWHM}}^2} \\
&\quad - \frac{1}{4(f_e + \Delta f)^2 + f_{\text{FWHM}}^2} \Bigg]
\end{aligned}
\tag{13}
$$

where we define $f_e = f_p - f_0$. Note that (13) describes the dispersion curve shown in Fig. 5(a). Its zero-crossing slope K_r is then calculated as

$$
\begin{aligned}
K_r &= V'_{\text{error}}|_{f_e=0} \\
&= R_r P_0 e^{-\alpha_0 L} \beta \cdot \frac{16 \Delta f}{(4\Delta f^2 + f_{\text{FWHM}}^2)^2}.
\end{aligned}
\tag{14}
$$

As a result, by setting $dK_r/d\Delta f = 0$, the optimum frequency deviation Δf that maximizes K_r is found to be

$$\Delta f_{\text{opt}} = \frac{f_{\text{FWHM}}}{2 \cdot \sqrt{3}} \approx 0.29 \cdot f_{\text{FWHM}}. \tag{15}$$

Inserting Δf_{opt} into (13), we also obtain the frequency offset $f_{e,\text{peak}}$ at which $V_{\text{error}}(f_e)$ reaches its peak value

$$f_{e,\text{peak}} = \frac{\sqrt{2 \cdot (\sqrt{13} - 1)}}{6} f_{\text{FWHM}} \approx 0.38 \cdot f_{\text{FWHM}}. \tag{16}$$

At this frequency point, the value of $V_{\text{error}}(f_e)$ is

$$V_{\text{error,max}} \approx 0.23 \cdot K_r \cdot f_{\text{FWHM}}. \tag{17}$$

ACKNOWLEDGMENT

REFERENCES

[1] W. J. Riley, "Handbook of frequency stability analysis," Nat. Inst. Standards Technol., Gaithersburg, MD, USA, NIST Special Publication 1065, 2008.

[2] (2017). Underwater Exploration With Chip Scale Atomic Clocks (CSAC). [Online]. Available: http://www.microsemi.com

[3] A. T. Gardner and J. A. Collins, "A second look at chip scale atomic clocks for long term precision timing," in Proc. OCEANS MTS/IEEE Monterey, Sep. 2016, pp. 1–9.

[4] R. Lutwak, "Principles of atomic clocks," in Proc. IEEE Int. Freq. Control Symp., San Francisco, CA, USA, May 2011, pp. 1–141.

[5] M. A. Lombardi, "Fundamentals of time and frequency," in The Mechatronics Handbook. Boca Raton, FL, USA: CRC Press, 2001, ch. 17.

[6] K. A. Sankaragomathi, J. Koo, R. Ruby, and B. P. Otis, "A ±3 ppm 1.1 mW FBAR frequency reference with 750 MHz output and 750 mV supply," in IEEE Int. Solid-State Circuits Conf. (ISSCC) Dig. Tech. Papers, Feb. 2015, pp. 1–3.

[7] B. J. Bloom et al., "An optical lattice clock with accuracy and stability at the 10^{-18} level," Nature, vol. 506, no. 7486, pp. 71–75, 2014.

[8] G. Alzetta, A. Gozzini, L. Moi, and G. Orriols, "An experimental method for the observation of r.f. transitions and laser beat resonances in oriented Na vapour," Il Nuovo Cimento B, vol. 36, no. 1, pp. 5–20, 1976.

[9] S. Knappe et al., "A microfabricated atomic clock," Appl. Phys. Lett., vol. 85, no. 9, pp. 1460–1462, 2004.

[10] R. Lutwak et al., "The chip-scale atomic clock—Low-power physics package," in Proc. 36th Annu. Precise Time Time Interval (PTTI) Meeting, Washington, DC, USA, 2004, pp. 339–354.

[11] S. Knappe, V. Gerginov, V. Shah, A. Brannon, L. Hollberg, and J. Kitching, "Long-term stability of NIST chip-scale atomic clock physics packages," in Proc. 38th Annu. Precise Time Time Interval (PTTI) Meeting, Washington, DC, USA, 2007, pp. 241–250.

[12] Quantum SA.54s Chip Scale Atomic Clock, Microsemi, Aliso Viejo, CA, USA, 2017.

[13] S. H. Yang, K. J. Baek, T. Y. Kwon, Y. B. Kim, and H. S. Lee, "Second-order zeeman frequency shift in the optically pumped cesium beam frequency standard with a dual servo system," Jpn. J. Appl. Phys., vol. 38, no. 10, pp. 6174–6177, 1999.

[14] D. A. Steck, "Cesium D line data," Theor. Division, vol. 4710, no. 7, pp. 1–31, 2008.

[15] C. Kulesa, "Terahertz spectroscopy for astronomy: From comets to cosmology," IEEE Trans. THz Sci. Technol., vol. 1, no. 1, pp. 232–240, Sep. 2011.

[16] J. Pereira et al., "Breath analysis as a potential and non-invasive frontier in disease diagnosis: An overview," Metabolites, vol. 5, no. 1, pp. 3–55, 2015.

[17] N. Sharma et al., "200–280GHz CMOS RF front-end of transmitter for rotational spectroscopy," in Proc. Symp. VLSI Technol. Circuits, Jun. 2016, pp. 1–2.

[18] C. Wang, B. Perkins, Z. Wang, and R. Han, "Molecular detection for unconcentrated gas with ppm sensitivity using 220-to-320-GHz dual-frequency-comb spectrometer in CMOS," IEEE Trans. Biomed. Circuits Syst., vol. 12, no. 3, pp. 709–721, Jun. 2018.

[19] K. Schmalz et al., "245-GHz transmitter array in SiGe BiCMOS for gas spectroscopy," IEEE Trans. THz Sci. Technol., vol. 6, no. 2, pp. 318–327, Mar. 2016.

[20] Q. Zhong, W. Choi, C. Miller, R. Henderson, and K. K. O, "A 210-to-305 GHz CMOS receiver for rotational spectroscopy," in IEEE Int. Solid-State Circuits Conf. (ISSCC) Dig. Tech. Papers, San Francisco, CA, USA, Jan./Feb. 2016, pp. 426–427.

[21] C. Wang and R. Han, "Dual-terahertz-comb spectrometer on CMOS for rapid, wide-range gas detection with absolute specificity," IEEE J. Solid-State Circuits, vol. 52, no. 12, pp. 3361–3372, Dec. 2017.

[22] C. Wang, X. Yi, J. Mawdsley, M. Kim, Z. Wang, and R. Han, "An on-chip fully electronic molecular clock based on sub-terahertz rotational spectroscopy," Nature Electron., vol. 1, no. 7, pp. 421–427, 2018.

[23] C. Wang, X. Yi, M. Kim, Y. Zhang, and R. Han, "A CMOS molecular clock probing 231.061-GHz rotational line of OCS with sub-ppb long-term stability and 66-mW DC power," in Proc. Symp. VLSI Technol. Circuits, Honolulu, HI, USA, Jun. 2018, pp. 113–114.

[24] C. H. Townes and A. L. Schawlow, Microwave Spectroscopy (Dover Books on Physics), 2nd ed. North Chelmsford, MA, USA: Courier Corporation, 2012.

[25] HITRAN: High-Resolution Transmission Molecular Absorption Database. [Online]. Available: http://hitran.org/

[26] A. G. Maki, "Microwave spectra of molecules of astrophysical interest VI. Carbonyl sulfide and hydrogen cyanide," *J. Phys. Chem. Reference Data*, vol. 3, no. 1, pp. 221–244, 1974.

[27] J. Vanier and L.-G. Bernier, "On the signal-to-noise ratio and short-term stability of passive rubidium frequency standards," *IEEE Trans. Instrum. Meas.*, vol. IM-30, no. 4, pp. 277–282, Dec. 1981.

[28] R. F. Lacey, A. L. Helgesson, and J. H. Holloway, "Short-term stability of passive atomic frequency standards," *Proc. IEEE*, vol. 54, no. 2, pp. 170–176, Feb. 1966.

[29] G. Y. Golubiatnikov, A. V. Lapinov, A. Guarnieri, and R. Knöchel, "Precise Lamb-dip measurements of millimeter and submillimeter wave rotational transitions of 16O 12C 32S," *J. Mol. Spectrosc.*, vol. 234, no. 1, pp. 190–194, 2005.

[30] G. Cazzoli and C. Puzzarini, "Sub-Doppler resolution in the THz frequency domain: 1 kHz accuracy at 1 THz by exploiting the Lamb-dip technique," *J. Phys. Chem. A*, vol. 117, no. 50, pp. 13759–13766, 2013.

[31] C. Wang and R. Han, "Rapid and energy-efficient molecular sensing using dual mm-Wave combs in 65 nm CMOS: A 220-to-320 GHz spectrometer with 5.2 mW radiated power and 14.6-to-19.5 dB noise figure," in *IEEE Int. Solid-State Circuits Conf. (ISSCC) Dig. Tech. Papers*, San Francisco, CA, USA, 2017, pp. 18–20.

[32] R. Xu, J.-Y. Lee, D. Y. Kim, S. Park, Z. Ahmad, and K. K. O, "0.84-THz imaging pixel with a lock-in amplifier in CMOS," in *Proc. IEEE Radio Freq. Integr. Circuits Symp. (RFIC)*, May 2016, pp. 166–169.

[33] C. Wang et al., "Robust sub-harmonic mixer at 340 ghz using intrinsic resonances of hammer-head filter and improved diode model," *J. Infr., Millim., Terahertz Waves*, vol. 38, no. 11, pp. 1397–1415, 2017.

[34] P.-Y. Chiang, Z. Wang, O. Momeni, and P. Heydari, "A 300 GHz frequency synthesizer with 7.9% locking range in 90 nm SiGe BiCMOS," in *IEEE Int. Solid-State Circuits Conf. (ISSCC) Dig. Tech. Papers*, vol. 57, Feb. 2014, pp. 260–261.

[35] R. Han et al., "A 320 GHz phase-locked transmitter with 3.3 mW radiated power and 22.5 dBm EIRP for heterodyne THz imaging systems," in *IEEE Int. Solid-State Circuits Conf. (ISSCC) Dig. Tech. Papers*, San Francisco, CA, USA, Feb. 2015, pp. 1–3.

[36] M. A. Koshelev, M. Y. Tretyakov, F. Rohart, and J.-P. Bouanich, "Speed dependence of collisional relaxation in ground vibrational state of OCS: Rotational behaviour," *J. Chem. Phys.*, vol. 136, no. 12, p. 124316, 2012.

[37] D. Ruffieux, M. Contaldo, J. Haesler, and S. Lecomte, "A low-power fully integrated RF locked loop for miniature atomic clock," in *IEEE Int. Solid-State Circuits Conf. (ISSCC) Dig. Tech. Papers*, Feb. 2011, pp. 48–50.

[38] D. J. Wineland, D. A. Howe, M. B. Mohler, and H. W. Hellwig, "Special purpose ammonia frequency standard a feasibility study," *IEEE Trans. Instrum. Meas.*, vol. IM-28, no. 2, pp. 122–132, Jun. 1979.

[39] B. Beuerle, J. Campion, U. Shah, and J. Oberhammer, "A very low loss 220–325 GHz silicon micromachined waveguide technology," *IEEE Trans. THz Sci. Technol.*, vol. 8, no. 2, pp. 248–250, Mar. 2018.

Xiang Yi (S'11–M'13) received the B.E. degree from the Huazhong University of Science and Technology (HUST), Wuhan, China, in 2006, the M.S. degree from the South China University of Technology (SCUT), Guangzhou, China, in 2009, and the Ph.D. degree from Nanyang Technological University (NTU), Singapore, in 2014.

From 2014 to 2017, he was a Research Fellow in NTU. He is currently a Post-Doctoral Fellow with the Massachusetts Institute of Technology (MIT), Cambridge, MA, USA. His research interests include radio frequency (RF), millimeter-wave (mm-wave), and terahertz (THz) frequency synthesizers, and transceiver systems.

Dr. Yi was a recipient of the IEEE ISSCC Silkroad Award and the SSCS Travel Grant Award in 2013. He is a Technical Reviewer of several IEEE journals and conferences.

James Mawdsley (S'17–M'18) received the S.B. degree in electrical engineering from the Massachusetts Institute of Technology (MIT), Cambridge, MA, USA, in 2018, where he is currently pursuing the M.Eng. degree in electrical engineering.

In 2017, he was with SpaceX, Irvine, CA, USA, where he designed RFICs for satellite communications. He is currently engaged in research into terahertz integrated circuit design.

Mina Kim (S'15–M'15) received the B.S. and M.S. degrees in electrical engineering from the Ulsan National Institute of Science and Technology, Ulsan, South Korea, in 2013 and 2016, respectively. She is currently pursuing the Ph.D. degree with the Massachusetts Institute of Technology (MIT), Cambridge, MA, USA.

Her research interests include clock generation and millimeter/terahertz-wave integrated circuit design.

Ms. Kim was a recipient of the MIT Electrical Engineering and Computer Science (EECS) Graduate Alumni Fellowship and the Kwanjeong Scholarship for the graduate study in 2017.

Zhi Hu (S'15) received the B.S. degree in microelectronics from Fudan University, Shanghai, China, in 2015. He is currently pursuing the Ph.D. degree with the Massachusetts Institute of Technology (MIT), Cambridge, MA, USA, with a focus on novel architectures of terahertz circuits.

Mr. Hu was a recipient of the SCSK Scholarship in 2013, the KLA-Tencor Scholarship in 2014, and the Best Student Paper Award (Second Place) of the IEEE Radio Frequency Integrated Circuits Symposium in 2017.

Cheng Wang (S'15) received the B.E. degree in engineering physics from Tsinghua University, Beijing, China, in 2008, the M.S. degree in radio physics from the China Academy of Engineering Physics, Mianyang, China, in 2011, and the M.S. degree in electrical engineering and computer science (EECS) from the Massachusetts Institute of Technology (MIT), Cambridge, MA, USA, in 2018, where he is currently pursuing the Ph.D. degree with the Department of EECS.

From 2011 to 2015, he was an Assistant Research Fellow with the Institute of Electronic Engineering, Mianyang. His research covers topics of millimeter/terahertz-wave gas spectroscopy, high-precision clock generation, wireless communication, and automotive radar.

Mr. Wang was a recipient of the Analog Device Inc., Outstanding Student Designer Award in 2016 and the IEEE Microwave Theory and Techniques Society Boston Chapter Scholarship in 2017.

Yaqing Zhang received the B.E. degree in optoelectronics from Nankai University, Tianjin, China, in 2012. He is currently pursuing the Ph.D. degree with the Department of Chemistry, Massachusetts Institute of Technology, Cambridge, MA, USA, under the supervision of Prof. K. A. Nelson.

His research topic covers linear and nonlinear terahertz spectroscopy, gas-phase rotational spectroscopy, and multi-dimensional terahertz spectroscopy.

Bradford Perkins received the B.A. degree in chemistry from the Dartmouth College, Hanover, NH, USA, in 2001, and the Ph.D. degree in chemical physics from JILA, University of Colorado Boulder, Boulder, CO, USA, in 2009, with a focus on investigation of dynamics at the gas–liquid interface.

In 2010, he was awarded a National Science Foundation Post-Doctoral Fellowship to work with the Chemistry Department, Massachusetts Institute of Technology (MIT), Cambridge, MA, USA, where he studied ultrafast processes in crystals and superconductors with terahertz (THz) spectroscopy. He is currently a Technical Staff Member with the Chemical, Microsystems, and Nanoscale Technologies Group, MIT Lincoln Laboratory, Lexington, MA, USA. His current research interests involve chemical and biological material sensing, aerosol chemistry, and novel laser-based spectroscopic techniques.

Ruonan Han (S'10–M'14) received the B.Sc. degree in microelectronics from Fudan University, Shanghai, China, in 2007, the M.Sc. degree in electrical engineering from the University of Florida, Gainesville, FL, USA, in 2009, and the Ph.D. degree in electrical and computer engineering from Cornell University, Ithaca, NY, USA, in 2014.

In 2012, he was an Intern with Rambus Inc., Sunnyvale, CA, USA. He is currently an Associate Professor with the Department of Electrical Engineering and Computer Science, Massachusetts Institute of Technology, Cambridge, MA, USA. His current research interests include microelectronic circuits and systems operating at millimeter-wave and terahertz frequencies.

Dr. Han is a member of the IEEE Solid-State Circuits Society and the IEEE Microwave Theory and Techniques Society. He was a recipient of the Cornell ECE Directors Ph.D. Thesis Research Award, the Cornell ECE Innovation Award, two Best Student Paper Awards of the IEEE Radio Frequency Integrated Circuits Symposium in 2012 and 2017, the IEEE Microwave Theory and Technique Society Graduate Fellowship Award, the IEEE Solid-State Circuits Society Predoctoral Achievement Award, MIT E. E. Landsman Career Development Chair Professorship in 1958, and the National Science Foundation (NSF) CAREER Award (winner) in 2017. He is an Associate Editor of the IEEE TRANSACTIONS ON VERY-LARGE-SCALE INTEGRATION (VLSI) SYSTEM and also serves on the Technical Program Committee (TPC) of IEEE RFIC Symposium and the Steering Committee of 2019 IEEE International Microwave Symposium (IMS).